Article

Drag Reduction by Riblets on a Commercial UAV

Lorenzo Cacciatori [1,†], Carlo Brignoli [1,†], Benedetto Mele [2], Federica Gattere [1], Celeste Monti [3] and Maurizio Quadrio [1,*]

1 Department of Aerospace Science and Technologies, Politecnico di Milano, 20133 Milan, Italy; lorenzo.cacciatori@mail.polimi.it (L.C.); carlo.brignoli@mail.polimi.it (C.B.); federica.gattere@polimi.it (F.G.)
2 Department of Industrial Engineering, University of Naples Federico II, 80138 Napoli, Italy; benmele@unina.it
3 Sky Eye Systems, 56021 Pisa, Italy; c.monti@skyeyesystems.it
* Correspondence: maurizio.quadrio@polimi.it
† These authors contributed equally to this work.

Abstract: Riblets are micro-grooves capable of decreasing skin-friction drag, but recent work suggests that additional benefits are possible for other components of aerodynamic drag. The effect of riblets on a fixed-wing, low-speed Unmanned Aerial Vehicle (UAV) on the total aerodynamic drag are assessed here for the first time by means of RANS simulations. Since the microscopic scale of riblets precludes their direct representation in the geometric model of the UAV, we model riblets via a homogenised boundary condition applied on the smooth wall. The boundary condition consists in a suitably tuned partial slip, which assumes riblets to be locally aligned with the flow velocity, and to possess optimal size. Several configurations of riblets coverage are considered to extract the potential for drag reduction of different parts of the aircraft surface. Installing riblets with optimal size over the complete surface of the UAV leads to a reduction of 3% for the drag coefficient of the aircraft. In addition to friction reduction, analysis shows a significant additional form of drag reduction localised on the wing. By installing riblets only on the upper surface of the wing, total drag reduction remains at 1.7%, with a surface coverage that is only 29%, thus yielding a significant improvement in the cost–benefit ratio.

Keywords: riblets; drag reduction; slip length

1. Introduction

The growing concern over energy efficiency and environmental pollution is furthering the appeal of transport vehicles, particularly aircraft, that produce less aerodynamic drag. One of the most interesting passive drag reduction techniques is the use of riblets, i.e., streamwise-aligned micro-grooves that are known to reduce turbulent skin-friction drag (see, for example, the review paper [1] and the many references therein), and are approaching usability in aeronautics.

Early studies, spurred by the oil crisis of the 1970s, were performed at NASA [2], and important experiments were carried out in the Berlin oil tunnel by Bechert and coworkers [3,4]. They evidenced the crucial importance of the riblet shape, their size, and—most importantly—the sharpness of their tip; optimal configurations empirically determined at the time yield up to 6–8% and possibly higher reductions in skin friction for low-*Re* flat plate-boundary layers studied in laboratory conditions. The theoretical understanding of the riblets working mechanism is due to Luchini [5], who quantified the different resistance offered by a grooved wall to the parallel flow and the cross-flow. He also explained [6] how skin-friction drag reduction is equivalent to an upward shift of the logarithmic portion of the turbulent velocity profile. This important argument, later taken up again by [7], implies that it is incorrect to describe riblets performance simply as a percentage change of the skin-friction coefficient, as this simplistic figure depends on the Reynolds number of the flow. However, the value of the upward shift, once measured in

viscous units, is Reynolds independent and should be used to characterize the ability of riblets (and other techniques) to reduce turbulent friction; in fact, recently this concept has been extended [8] to other strategies of skin-friction reduction.

To capture, in a numerical simulation, the complex physics of the interaction between turbulence and a solid wall covered by riblets, and to properly measure friction reduction, direct numerical simulations (DNS) or wall-resolved large eddy simulations (LES) are required. Such computations are unfeasible for complex aeronautical configurations at high Reynolds numbers, where numerical simulations based on the Reynolds-Averaged Navier–Stokes equations (RANS) equipped with a turbulence model are the standard approach. Owing to their microscopic dimensions, however, riblets on an aircraft cannot be included directly in a RANS simulation. Even if they could, it is unclear to what extent a standard RANS model would be able to represent the physics of drag reduction.

Bridging the gap between drag reduction by riblets in turbulent flows and the need to incorporate it into RANS-type flow solvers has led to the development of computational models for riblets. Aupoix et al. [9] modified the Spalart–Allmaras turbulence model to account for riblets by using smooth-wall geometry. Along similar lines, Mele et al. [10] introduced a modified boundary condition for the $k - \omega$ turbulence model, and Koepplin et al. [11] extended the Aupoix model to describe riblets locally misaligned with the mean flow, and to account for mean pressure gradients.

How riblets affect a turbulent boundary layer with a non-zero pressure gradient is a debated subject [12–14]. In 2018, Mele and Tognaccini [15] developed a new model based on a slip-length concept, whose results provided an interesting view on the riblets drag reduction mechanism in presence of pressure gradients. In addition to friction reduction, they found that riblets alter the pressure distribution, and may provide additional pressure drag reduction. This indirect effect was also observed for other friction-reduction devices: Banchetti et al. [16] used spanwise forcing to reduce turbulent friction on a wall with a bump, and found in their incompressible DNS study that a reduced friction drag is accompanied by a reduced pressure drag. Similarly, using DNS, Quadrio et al. [17] studied the compressible flow over a wing, and observed how spanwise forcing affects the shock wave to yield large reduction of the total drag of the aircraft. The availability of a boundary condition to faithfully simulate in a RANS the presence of riblets on the surface of a solid body of complex shape is thus becoming extremely attractive.

The standard no-slip condition at a solid wall can be extended to a partial-slip one, which is useful to describe specific physical situations (e.g., flow over superhydrophobic surfaces). Riblets are amenable to such a description; their slip length is related to the protrusion height concept [3–5]. In particular, Luchini in [5] defined the longitudinal and transverse protrusion heights, which identify the virtual origin for the streamwise and spanwise velocity profiles, and realised that the only meaningful non-arbitrary quantity is their difference. Later, he also introduced [18] a linearised boundary condition for generic roughness and the protrusion heights for various roughness types to be adopted in DNS. He also demonstrated that the difference Δh between the two riblets protrusion heights corresponds to the slip length λ. Gomez de Segura et al. [19] later discussed how the slip length λ^+ expressed in viscous units is equivalent to the upward displacement ΔU^+ of the mean velocity profile in the logarithmic region; here, $\lambda^+ = \lambda u_\tau / \nu$, where ν is the kinematic viscosity, $u_\tau = \sqrt{\tau_w / \rho}$ is the friction velocity, ρ is the density, and τ_w is the (local) shear stress.

The value of the slip length λ depends upon the shape and size of the riblets cross-section. Bechert et al. [4] found that the largest drag reduction for riblets of different shapes was obtained when s^+, the spanwise period of the riblets, is in the range 10–20. García-Mayoral and Jiménez [1] tested alternative scalings to find whether drag reduction can be linked to a single geometric parameter that captures the importance of riblet spacing and their cross-sectional shape as well. Data for different riblets were found to best collapse when plotted against a dimensionless length scale l_g^+ derived from the cross-sectional area A_g of the groove, and defined as $l_g^+ = (A_g^+)^{1/2}$. For riblets of various geometries, the best

performance was consistently found at $l_g^+ \approx 10.5$. For optimal triangular riblets, $l_g^+ = 10.5$ corresponds to a unitary shift ΔU^+, which coincides with the one reported in previous studies [15,20,21]. Recently, Zhang et al. [22] have been able to compute the slip length for other riblets shapes, i.e., with trapezoidal and blade cross-sections.

The goal of this paper is to present the implementation of a slip-length boundary condition for riblets, and to use it in a set of RANS simulations to assess the drag reduction capabilities of riblets when installed on a fixed-wing UAV, for which endurance is of capital importance. Indeed, over the years, riblets have been studied either at low speed over plane walls, or in transonic flow conditions for aeronautical applications, especially for medium- or long-range commercial passenger aircraft. Such studies, carried out both numerically [10,23] and experimentally [24–28], provide interesting results for aircraft operating in a range of chord-based Reynolds numbers up to $Re_\infty = 3 \times 10^7$. In contrast, the low-speed aircraft considered in the present work has a cruise speed of 22 m/s with $Re_\infty = 5 \times 10^5$.

This paper describes the implementation into an incompressible CFD solver of a slip-length wall boundary condition, similar to that described in ref. [21], to compute the drag reduction achievable with riblets of optimal dimensions. The computational model is validated against configurations of increasing complexity, and eventually applied to a realistic use case. We also consider selective deployment of riblets to different parts of the aircraft to show that drag reduction is not trivially proportional to the surface area covered by riblets. The structure of the work is as follows. After this introduction, Section 2 describes our model and the computational setup; Section 3 contains the results of preliminary simulations intended for validation; the actual results are described in Section 4, and Section 5 contains a concluding discussion.

2. Methods

2.1. Slip Length Boundary Condition

Both theory and experiments [3–5] suggest that the physics involved in drag reduction by riblets acts through a local mechanism. Indeed, since riblets are small compared to the turbulent structures of the near-wall cycle, far enough from the wall, the turbulent flow perceives the presence of riblets only as a homogeneous effect: the upward shift $\Delta U^+ > 0$ of the logarithmic portion of the mean velocity profile:

$$U^+ = \frac{1}{\kappa} \log(y^+) + A + \Delta U^+ \tag{1}$$

where $\kappa = 0.392$ is the von Kármán constant, and $A = 4.48$ is the near wall intercept for smooth surfaces (these constants are set after [29], but their numerical value does not affect the outcome of the study). The dimensionless vertical shift ΔU^+ equals the virtual shift in wall units of the non-slipping wall [4], i.e., the slip length λ^+. We exploit this shift to account for the presence of riblets via a slip boundary condition, which linearly relates the wall value of the longitudinal component of the velocity u_w (the subscript w indicates quantities evaluated at the wall) to the wall shear rate $(\partial u / \partial y)_w$ through the slip length λ:

$$u_w = \lambda \left(\frac{\partial u}{\partial y} \right)_w, \tag{2}$$

thus effectively recovering the no-slip condition when $\lambda = 0$. The discrete counterpart of Equation (2), where the derivative is approximated with a finite difference, reads:

$$u_w = \lambda \frac{u_1 - u_w}{d}, \tag{3}$$

where u_1 is the longitudinal velocity at the first inner mesh point, and d is its distance from the wall. Hence, the velocity at the wall is:

$$u_w = u_1 \frac{\lambda}{\lambda + d}. \tag{4}$$

In this work, we always set the shift of the mean velocity profile at $\Delta U^+ = 1$, which corresponds [15,20,21] to the best-performing riblets with triangular cross-section. These riblets have a square root of the cross-sectional area of $l_g^+ = 10.5$, and provide a drag reduction of 7% when measured in the lab under controlled conditions and at low *Re*. Using $\Delta U^+ = 1$ implies setting $\lambda^+ = 1$, whence the physical size of the riblets varies along the body with the friction velocity of the flow. In other words, riblets are assumed to be locally optimal everywhere, and the corresponding physical dimensions are computed as a result of the simulation.

It is worth noticing that the present boundary condition can be used to simulate, besides riblets, any other drag reduction method whose effect reduces to a shift in the mean velocity profile. To this purpose, only the slip-length value must be adjusted.

2.2. Computational Setup

The boundary condition described above has been implemented in OpenFOAM [30], an open-source finite-volumes CFD library widely used in engineering and science, both in commercial and academic studies. Before considering the UAV, the boundary condition has been validated on flow cases of increasing complexity where at least partial information is available for comparison: a flat plate and a NACA 0012 airfoil.

The selected flow solver is SimpleFOAM, which uses the SIMPLE (Semi-Implicit Method for Pressure-Linked Equations) algorithm to solve the incompressible steady RANS equations. The $k - \omega$ SST turbulence model [31] has been adopted in this work, where standard values for the coefficients and no transition model have been used. For all the simulations, we adopt a freestream ratio between eddy and laminar viscosity equal to 0.001, together with free-stream turbulence intensity of $TU_\infty = 5\%$, with the only exception of the flat plate case, for which $TU_\infty = 0.5\%$. The spatial discretization used for the divergence, gradient, and Laplacian operators is second-order accurate. All the results have been checked to be fully converged in integral quantities (drag and lift) and in the residuals, by ensuring that the L_1 norm reduced to 10^{-8} times the initial value of the residual.

The study considers three geometries of increasing complexity. The first case is a two-dimensional flat plate boundary layer of length $L = 2$ m is considered, where $Re = U_\infty L/\nu = 10^6$. With air as working fluid, and a free-stream velocity of $U_\infty = 5$ m/s, the computational domain is rectangular and extends for 2.3 m in length and 1 m in height. The flat plate sits along the lower boundary of the computational domain. The domain extends 0.3 m upstream of the flat plate, and a symmetry boundary condition is used to simulate a free stream approaching the plate in this region. A suitable volume mesh is designed with the BlockMesh utility available in OpenFoam, and checked to yield mesh-independent results with a mesh sensitivity study. The final mesh, which provides a local friction coefficient that does not vary with further refinements, consists of 125,000 hexahedral elements, with 250 cells in the wall-normal direction and 500 cells in the wall-parallel direction, of which 400 are distributed over the flat plate. Non-uniform grid spacing is adopted to obtain more resolution in the near-wall and in the leading-edge regions, to better capture the boundary-layer development. Transition is adequately described, and the distance y_1 of the first cell from the wall is always below unity when expressed in wall units, i.e., $y_1^+ < 1$.

The second case is a two-dimensional NACA 0012 airfoil, at a chord-based Reynolds number of $Re_\infty = 10^6$. The airfoil chord c is taken of unitary length at 1 m, and the far-field boundary is located approximately $50c$ away from the airfoil surface. A mesh sensitivity study is carried out on a number of C-type grids by observing changes in the drag coefficient after successive mesh refinements. The chosen grid consists of 450 hexahedral cells in the chord-normal and 725 in the chord-tangent directions, and provides a repeatable transition

location. The mesh spacing near the airfoil is sufficient to ensure $y^+ < 1$ over the airfoil surface. Stretching of the grid is used to improve resolution in the wake region. To further validate the mesh accuracy, the solution has also been checked as a function of the angle of attack α. Hence, a number of preliminary runs at various values of α have been performed, without riblets, by replicating the flow conditions used in [32]. The outcome in terms of lift and drag coefficients is in very good agreement with the results reported by [32], as well as with the experimental measurements described in [33].

The final and most important case is the UAV. With a total length of 2.4 m and wing span of 3.6 m; its (simplified) geometry is described in some detail in Section 2.3. Simulations are carried out first on the isolated UAV wing, to understand to what extent the indirect beneficial effects of riblets noticed for the NACA 0012 carry forward to three dimensions, and the complete UAV is then considered. In both cases, the computational domain is made by a hemisphere, with a radius of 50 m that surrounds the wing half-span and the UAV half-span mounted on the $x - z$ plane, respectively. Symmetry is used to reduce computational cost. In this case, a commercial mesher is used to create unstructured meshes made by hexahedral and tetrahedral cells, with refinements boxes to capture the flow development near the body and in the wake. The grids possess 24 additional layers of hexahedral and tetrahedral elements aligned to the boundary surface, to guarantee that $y_1^+ < 1$, thus satisfying the requirements for an accurate computation inside the boundary layer within a low-Re formulation that does not resort to wall functions or other models of the near-wall region. A suitable mesh density is determined by observing changes in the drag coefficient, and robustness in predicting transition. The final mesh is designed with 4 million elements for the wing and 9.6 million elements for the full UAV.

2.3. The UAV Model

The considered UAV belongs to the family of Mini and Light Tactical UAV, with a MTOW (maximum take-off weight) ranging from 25 to 50 kg. The UAVs of this class are designed to integrate multiple payloads with different capabilities, e.g., EO/IR sensors, multi/hyperspectral cameras, LiDAR, transmitters, and radars. Flexibility is ensured by the fuselage modularity and by the possibility of changing the onboard systems configuration to achieve an optimised aircraft balance.

In this work, we consider a simplified geometric model of the UAV, as plotted in Figure 1, where small-scale geometric details and the propeller are omitted. The motivation is two-fold: such a simplified geometry, while remaining representative of the actual aircraft and retaining its essential qualitative features and dimensional characteristics, is free from intellectual property constraints; moreover, the lack of small-scale details allows some savings of computational effort. The simplified UAV is 2.4 m long and it has a span $b = 3.6$ m. It has a swept wing with a chord length of 0.3 m at the root with winglets at the tips of 0.22 m and dihedral angle of $21.5°$. The considered reference surface area is $S = 1$ m^2. The UAV is characterised by a reverse V tail made by a symmetric four-digit NACA airfoil with a span of 1.05 m and a chord of 0.23 m. The tail is directly connected to the lower surface of the wing by two booms of 1.05 m with a circular cross-sectional area of radius 0.015 m. The fuselage is 1.41 m long and its cross-section originates from a rectangular shape, 0.29 m high and 0.23 m wide, with rounded edges. The drone cruise speed is 22 m/s, leading to a chord-based Reynolds number $Re_\infty = 5 \times 10^5$. The UAV weight of 25 kg and the cruise speed of 22 m/s, together with the geometrical information mentioned above, imply a lift coefficient in cruise of $C_L = 0.8322$.
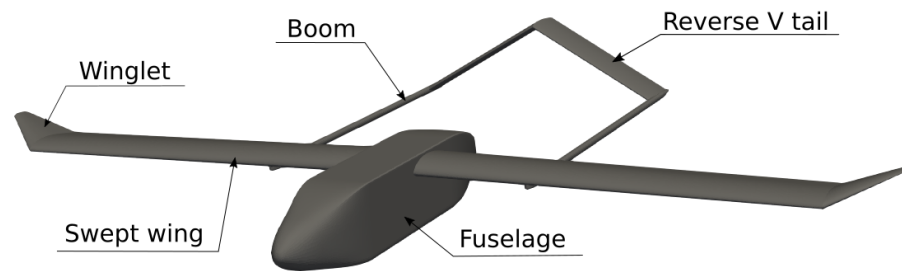
Figure 1. CAD model of the simplified UAV.

2.4. Dimensionless Force Coefficients

In this paper, the aerodynamic coefficients, i.e., the ratio of a force component and the reference quantity $1/2\rho U_\infty^2$, are the lift coefficient C_L and the total drag coefficient C_D. The latter can be decomposed into friction $C_{D,f}$ and pressure $C_{D,p}$ drag coefficients; the former describes the resistance to the relative motion between the fluid and the solid boundary due to viscous effects, the latter quantifies the net drag force arising from pressure variation around the body. When a wing of finite span is considered, the drag coefficient can alternatively be decomposed into induced and profile drag coefficients. The former, defined as $C_{D,i} = C_L^2/(\pi b^2/S)$ describes the additional drag due the three dimensional effects cause by the lift, and the latter, defined as $C_{D,pr} = C_D - C_{D,i}$ describes the same quantity due to all the other types of drag except that which is lift induced. Profile drag can further be decomposed in friction drag $C_{D,f}$ and form drag $C_{D,form} = C_{D,pr} - C_{D,f}$. Lastly, the local skin-friction and pressure coefficients are defined as $C_f = 2\tau_w/\rho U_\infty^2$ and $C_p = 2p/\rho U_\infty^2$ (in the coefficient subscripts, capital letters indicate global quantities and small letters indicate local quantities).

Changes between clean and riblets configurations are computed as $\Delta C_x = C_{x,0} - C_x$, where the subscript 0 refers to the clean configuration and x is the quantity of interest. The drag reduction rate, i.e., the change in drag normalised with the drag of the clean configuration is defined as $\Delta C_D/C_{D,0}$.

3. Validation

The boundary condition used to model riblets is first tested on simple two-dimensional flows, where available information allows a quantitative check of the outcome.

3.1. Flat Plate

The first application example is the zero-pressure gradient boundary layer developing over a flat plate. Optimal V-shape riblets, with $l_g^+ = 10.5$ corresponding to $h^+ = \sqrt{2}l_g^+$, are placed everywhere along the plate, immersed in a uniform external flow.

Figure 2 (left) shows how riblets influence the streamwise evolution of the friction coefficient, demonstrating the correct amount of drag reduction. On the entire plate, the integrated percentage drag reduction is $\Delta C_D/C_{D,0} = 6.5\%$, in agreement with existing experimental [3] information. Local changes of C_f, descending from the imposed slip, are consistent with those by ref. [15]. The evolution of the physical dimensions of the grooves is shown in Figure 2 (right), together with the analogous evolution of the slip length. Once the boundary layer becomes fully turbulent, i.e., for $Re_x > 10^5$, changes of the slip length with the streamwise coordinate are rather mild: there is a small increase with Re_x to reach the largest value of 50 microns at the downstream end of the plate. By construction, as explained earlier in Section 2, this corresponds to one viscous length. At the plate end, the predicted size of optimal riblets is approximately $h = 0.8$ mm.

The correctness of the model is directly checked in Figure 3, which provides graphical evidence that, regardless of the streamwise location, the upward shift of the mean velocity profile is of unitary value, confirming that $\Delta U^+ = \lambda^+ = 1$.

3.2. NACA 0012 Airfoil

Testing progresses to consider the two-dimensional flow around a NACA 0012 airfoil; this test case remains highly simplified, but brings in pressure drag, and thus lends itself to studying the effect of riblets on this non-frictional drag component. Unfortunately, little information is available for validation.

Once again, the airfoil is assumed to be fully covered by riblets of locally optimal size, i.e., ensuring $l_g^+ = 10.5$ everywhere. Figure 4 shows the mean velocity profile on the upper surface of the airfoil at $x/c = 0.5$, for two different angles of attack, namely 0 and 4 degrees. The expected unitary upward shift ΔU^+ due to the grooves is consistently observed. At $\alpha = 4°$, experimental data are available from ref. [34], and the present results appear to agree with them. However, the agreement is less satisfactory at other incidences. It must be mentioned that experiments were carried out with riblets of constant physical size, with a size that is about 10 viscous lengths. The percentage total drag reduction at $\alpha = 0°$ is measured to be 7%, which is in agreement with the experimental data from ref. [34,35], as well as with CFD results obtained by Mele and Tognaccini in [32]. Our data indicate only a mild variation of drag reduction with the angle of attack, while ref. [35] mentions an increase beyond 16% at $\alpha = 0°$ and a sudden drop to zero at $\alpha = 10°$. The lower part of Figure 4 compares the evolution of the skin-friction coefficient along the airfoil, and shows very good agreement with the same quantity taken from ref. [32] (except for the precise location of the transition region).
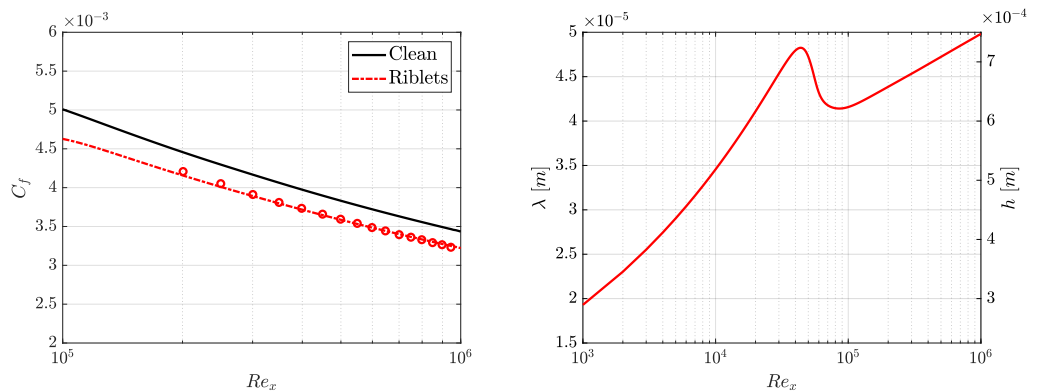

Figure 2. Zero-pressure-gradient boundary layer over a flat plate. **Left**: evolution of the skin-friction coefficient with/without riblets, and comparison with data from ref. [15]; **right**: change along the plate of the slip length (**left** y axis) and riblets height (**right** y axis), in dimensional units.
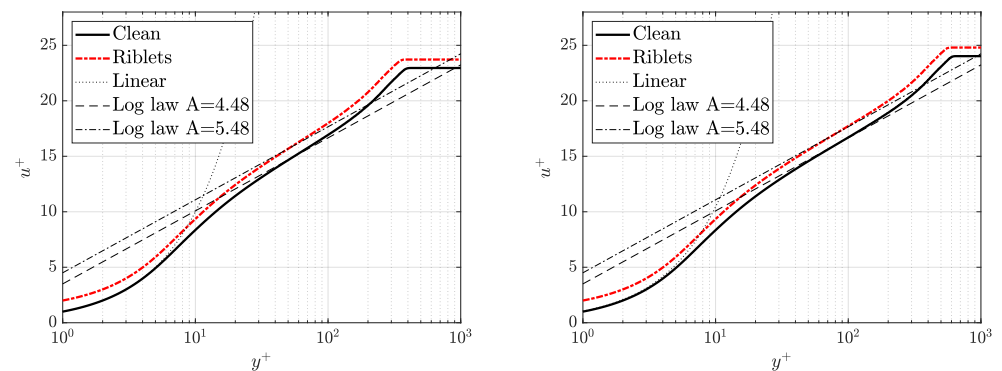

Figure 3. Mean velocity profile with/without riblets over the flat plate, at $Re_x = 5 \times 10^5$ (**left**) and $Re_x = 9 \times 10^5$ (**right**). The riblets profile consistently shows the upward shift of $\Delta U^+ = 1$ on the logarithmic region.

The pressure coefficient C_p and the difference $\Delta C_p = C_{p,0} - C_p$ at $\alpha = 4°$ are shown in Figure 5. Changes are visible, to attest once again the effect of riblets on the pressure

distribution along the airfoil. Changes in the expansion peak at the leading edge and on the pressure recovery at the trailing edge due to riblets provide a significant additional contribution to drag reduction; form drag is reduced by 7.7%, adding to the friction reduction of 6.7%. These results agree with several findings by Mele and Tognaccini [15], who interpreted the reduced form drag by observing that riblets change the flow field by making it more similar to the inviscid solution, where the slip length is infinite, and form drag is exactly zero. Moreover, the altered pressure distribution leads to a larger lift in all tested incidences; this effect, which will be discussed later when discussing the full aircraft, is important for the reduction of the total drag: since the aircraft in cruise always needs the same lift, increased aerodynamic efficiency implies a reduced angle of attack in cruise, thus bringing in an additional contribution to drag reduction.
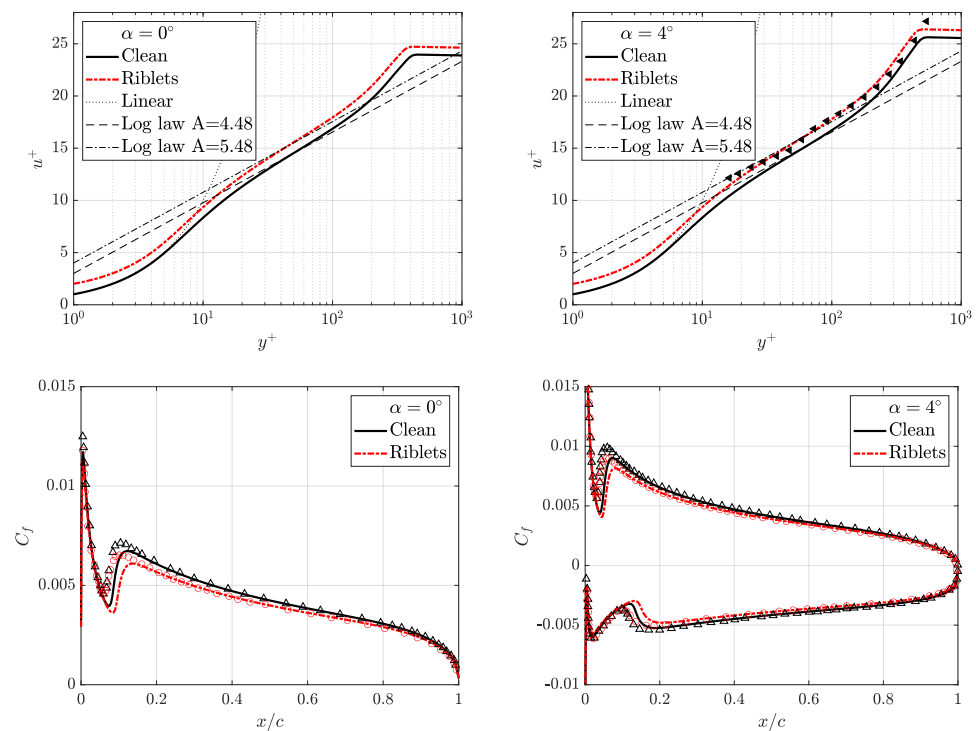
Figure 4. Mean velocity profiles (**top**) and skin-friction coefficient (**bottom**) for the NACA0012 airfoil, at an incidence of $\alpha = 0°$ (**left**) and $\alpha = 4°$ (**right**). The **top row** shows the mean profile over the suction side in law-of-the-wall form at $x/c = 0.5$, and compares with data from ref. [34]. The **bottom row** plots the evolution of the friction coefficient along the chord, and compares with data from ref. [32], represented with symbols.
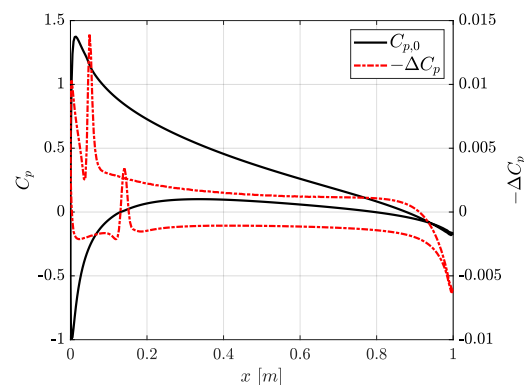
Figure 5. Pressure coefficient on the pressure and suction sides of the NACA0012 airfoil at $\alpha = 4°$ for the clean case (black line), and difference with the riblets case (red dashed line).

4. Results

4.1. The Isolated UAV Wing

The UAV wing is considered first, to focus on the presence of indirect drag reduction effects in three dimensions, but without the geometrical complexities implied by the interaction between wing and fuselage. The UAV finite isolated wing is considered at the cruise flight condition of $Re_\infty = 5 \times 10^5$. As always, locally optimal riblets with $l_g^+ = 10.5$ are placed over the entire wing surface.

Figure 6 shows how drag reduction induced by riblets changes with the angle of attack. The friction component of the total drag reduction is nearly constant at 6.3%, whereas pressure and total drag change with α. At $\alpha = 0°$, the total drag reduction rate is 3.7%, and diminishes at larger incidences. Clearly, the diminished total drag reduction goes hand in hand with the diminished pressure drag reduction. As already observed for the NACA 0012 airfoil in Section 3.2, riblets tend to modify the pressure distribution in such a way that lift is increased; this is confirmed here for the UAV wing. This phenomenon causes an increase in the lift-induced drag, which is not seen in two dimensions. This should not be regarded as a negative effect of riblets, since the aircraft has to achieve the same lift, and increased aerodynamic efficiency is always beneficial.
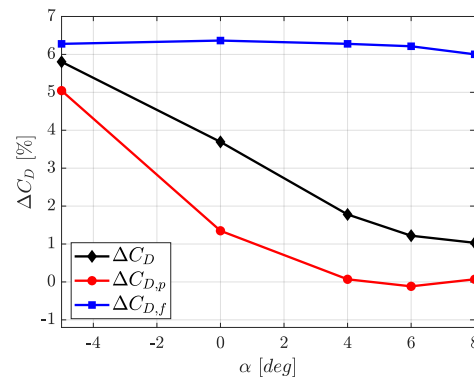

Figure 6. Riblets drag reduction vs. angle of attack for the UAV wing.

In fact, riblets' performance should be measured by adjusting α in such a way that the lift coefficient is unchanged. In Table 1, we compare the clean case and the riblets case at the same angle of attack, and at the same lift coefficient as well. Two configurations are considered, at a nominal angle of attack of $\alpha = 0°$ and $\alpha = 4°$. Total drag is split into friction $C_{D,f}$ and pressure $C_{D,p}$ drag, as well as induced $C_{D,i}$ and profile $C_{D,pr}$ drag. As expected, comparing at the same C_L provides larger drag reduction than comparing at the same α. At the same angle of attack, riblets produce a larger lift coefficient, and hence, a larger induced drag. It is worth noticing that the decrease in $C_{D,pr}$ is almost the same for the cases at constant α and constant C_L, whereas the induced drag is larger when compared at the same α.

Table 1. Aerodynamic coefficients for the isolated UAV wing. Comparison between clean and riblets configurations is carried out at the same angle of attack and at the same lift coefficient for nominal angle of attack of $\alpha = 0°$ and $\alpha = 4°$.

	Clean	Riblets		Clean	Riblets	
	$\alpha = 0°$	$\alpha = 0°$	$\alpha = -0.0626°$	$\alpha = 4°$	$\alpha = 4°$	$\alpha = 3.885°$
C_L	0.4996	0.5055 (+1.2%)	0.4996 (-)	0.8719	0.8828 (+1.8%)	0.8719 (-)
C_D	0.0227	0.0219 (−3.7%)	0.0217 (−4.5%)	0.0386	0.0380 (−1.8%)	0.0374 (−3.3%)
$C_{D,p}$	0.0121	0.0119 (−1.4%)	0.0118 (−2.8%)	0.0280	0.0280 (-)	0.027 (−2.2%)
$C_{D,f}$	0.0106	0.0099 (−6.4%)	0.0099 (−6.4%)	0.0106	0.0100 (−6.3%)	0.0100 (−6.3%)
$C_{D,i}$	0.0077	0.0079 (+2.4%)	0.0077 (-)	0.0235	0.0241 (+2.5%)	0.0235 (-)
$C_{D,pr}$	0.0150	0.0140 (−6.8%)	0.0140 (−6.8%)	0.0151	0.0138 (−8.4%)	0.0138 (−8.5%)

Drag breakdown is graphically shown at various α in Figure 7: the focus is on the total, induced, and profile drag on the left panel, and on the contributions to profile drag on the right panel. From the left panel, riblets are seen to mainly act on the profile drag, while the lift-induced drag is essentially unchanged. The right panel of Figure 7 focuses on the decomposition of profile drag, and shows that, besides the obvious reduction of friction drag, riblets additionally act upon form drag in a significant way. Depending on the angle of attack, the benefit of riblets in reducing $C_{D,pr}$ is in the 5–10% range. This is linked to the modifications on the pressure distribution on the wing, already observed in the NACA 0012 validation tests; see Figure 5. The pressure distribution at $2y/b = 0.52$ for the UAV wing is shown in Figure 8, and confirms the larger pressure recovery and the increased expansion peak induced by riblets that are at the root of form drag reduction.
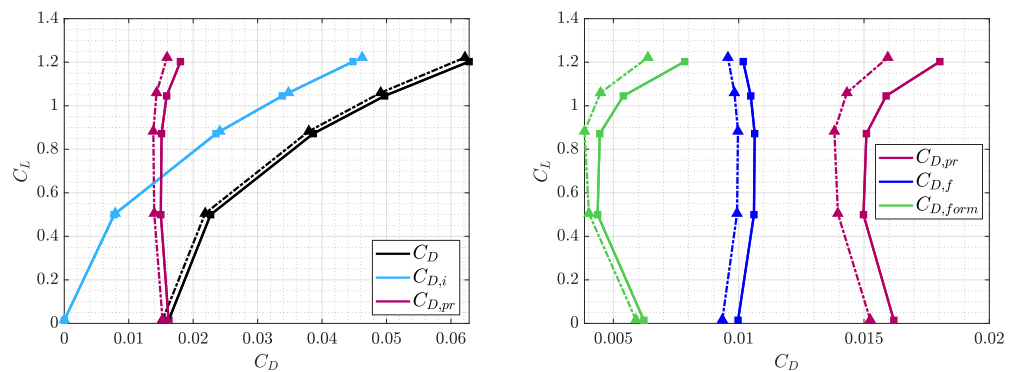

Figure 7. Drag breakdown for the isolated UAV wing (**left**), and focus on the profile drag (**right**). Solid lines with square markers indicate the clean configuration; dashed lines with triangular markers indicate the configuration with riblets.

Finally, Figure 9 plots the skin friction distribution at the spanwise station $2y/b = 0.52$ of the wing, and compares clean and riblets configurations at different angles of attack. A decrease in the skin friction across the entire chord is observed. In particular, on the suction side friction is mainly reduced in the fore portion; at large angles of attack, friction reduction vanishes in the aft part. On the lower surface, the reduction in friction is almost constant when α is varied.

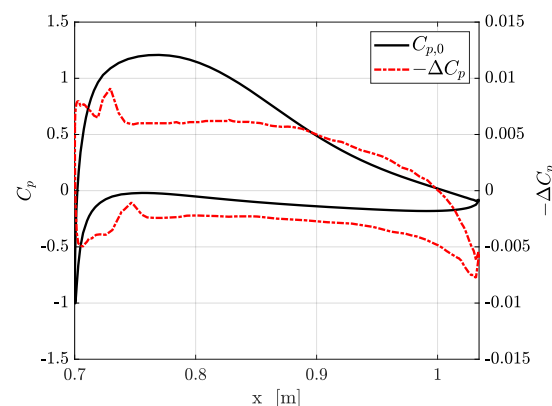**Figure 8.** Pressure coefficient on the pressure and suction sides of the isolated UAV wing at $2y/b = 0.52$, at $\alpha = 4°$, for the clean case (black line) and difference with the riblets case (red dashed line).

4.2. The UAV

The complete UAV is now considered in the configuration described above and shown in Figure 1. Consistently with the rest of this study, riblets are assumed to be locally optimal,

with $l_g^+ = 10.5$ and unitary slip length $\lambda^+ = 1$. The spatial distribution of the optimal riblet size, i.e., l_g (which, for a given cross-sectional shape, leads immediately to the geometric dimensions of the riblets) is retrieved as a result of the simulations. It should be remarked, however, that previous work [10] indicates how the size of locally optimal riblets does not vary much, so that the drag reduction obtained adopting riblets with constant physical size is quite near to the maximum drag reduction.

A series of simulations with/without riblets is carried out to provide data points to build the polar of the aircraft (Figure 10). Owing to the already highlighted lift increase provided by riblets, the angle of attack necessary to provide the required lift in cruise conditions slightly decreases from $\alpha = 2.85°$ to $2.81°$. The drag reduction obtained for the entire aircraft is an interesting 3%, which derives from a combination of a (less important) friction drag reduced by 6.1% and a (more important) pressure drag reduced by 1.5%.
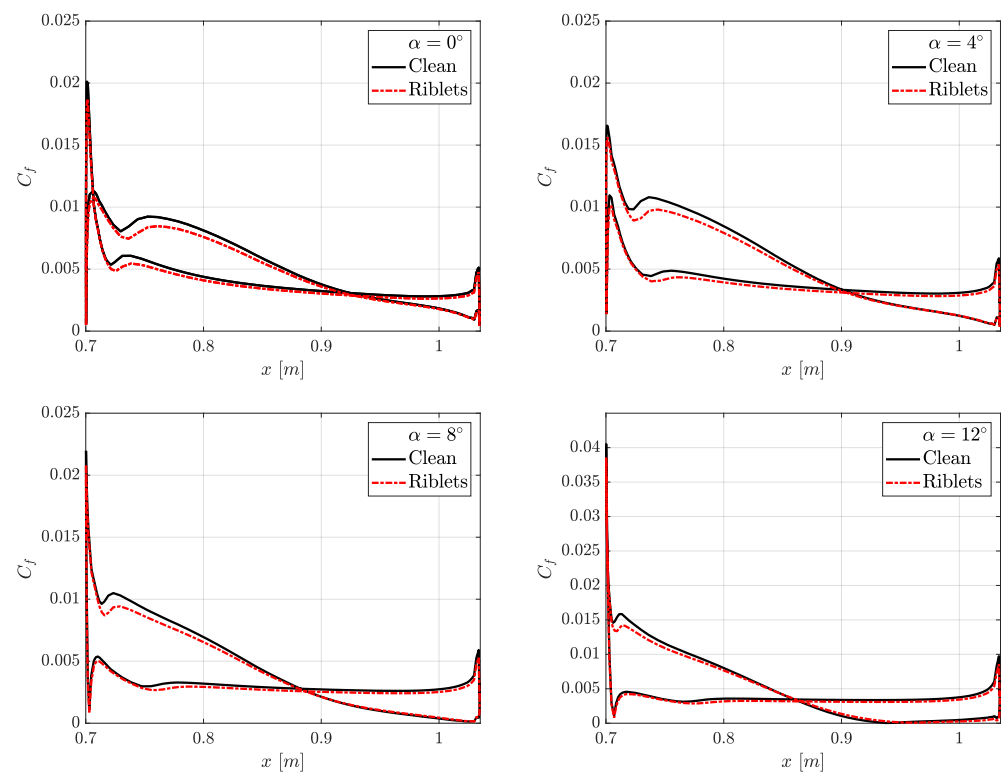

Figure 9. Friction coefficient for the isolated UAV wing, at spanwise location $2y/b = 0.52$ and four angles of attack.
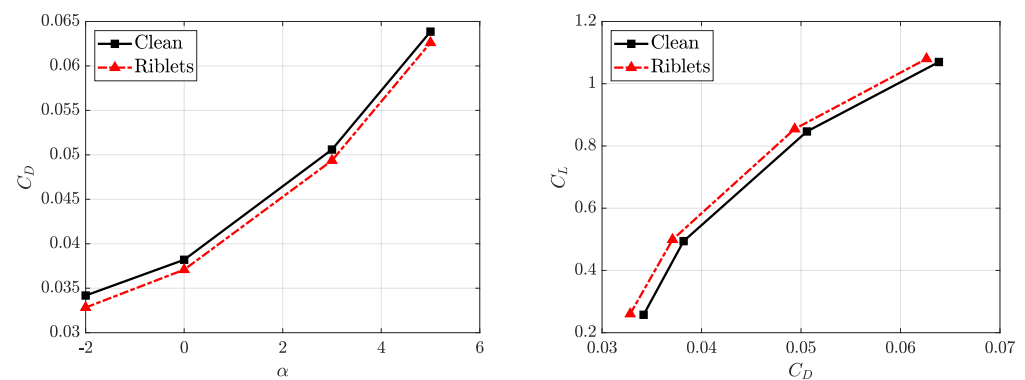

Figure 10. $C_D(\alpha)$ and polar curves of the UAV, in clean/riblets configurations.

Figure 11 helps determining where the largest percentage changes of the skin friction take place over the surface of the aircraft. $\Delta C_f/C_{f,0}$ is about 6% almost everywhere, roughly

as expected for a flat plate at this value of *Re*, except for the region near the trailing edge and for the aft part of the fuselage: here, the absolute value of C_f approaches zero, and its percentage variations become less meaningful.
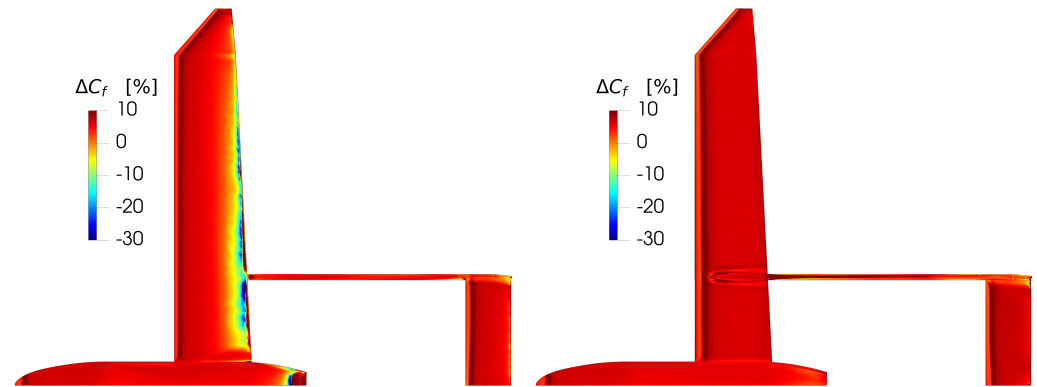

Figure 11. Percentage of skin friction reduction on the upper (**left**) and lower (**right**) parts of the aircraft in cruise condition.

Figure 12 shows the computed height distribution for the locally optimal riblets, by assuming that the cross-sectional riblet shape is a standard V groove, for which $s^+ = h^+ = \sqrt{2}l_g^+$. The optimal riblets height is about 0.2 mm nearly everywhere, except for the trailing edge of the wing, and for the aft part of the fuselage. This provides graphical evidence for the previous statement that riblets of properly chosen constant physical height would provide drag reduction that is very close to the maximum.

Riblets are then tested in off-design situations, i.e., at various incidences different from the cruise angle of attack, to check for robustness and to verify that riblets do not cause unwanted effects on the UAV aerodynamics during manoeuvrers or the climb/descent phases of a typical mission. As already noted for the UAV wing, Figure 13 shows that, although drag reduction is maximum in cruise, the performance degrades only mildly when the angle of attack differs from the cruise value. Again, it is confirmed that friction drag reduction remains nearly constant when α ranges from $-2°$ to $5°$.
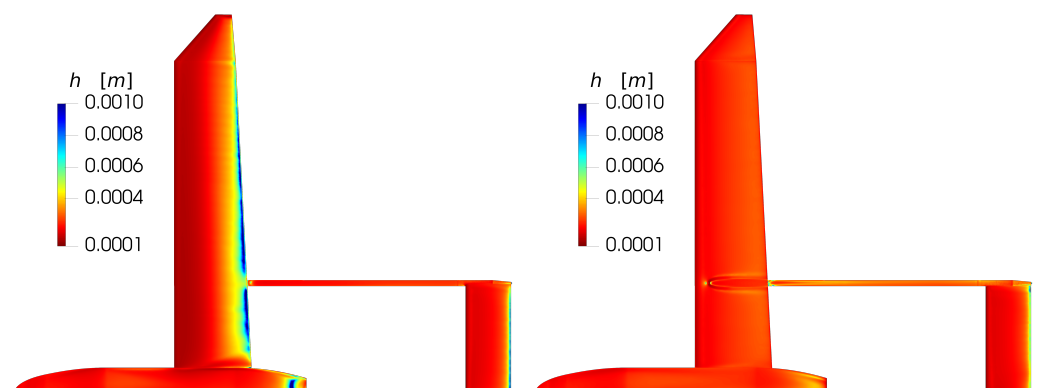

Figure 12. Spatial distribution of the computed optimal riblets height in physical units, for symmetric V groove riblets. **Left**: upper part of the aircraft in cruise conditions; **right**: lower part.

Finally, the aerodynamic drag is broken down into profile drag and induced drag in the left plot of Figure 14, while the right plot decomposes further profile drag into friction and form drag. The most obvious difference between clean and riblets configurations is the reduced profile drag, which derives from a sizable reduction in the friction component, joint with a comparable contribution from the form drag.
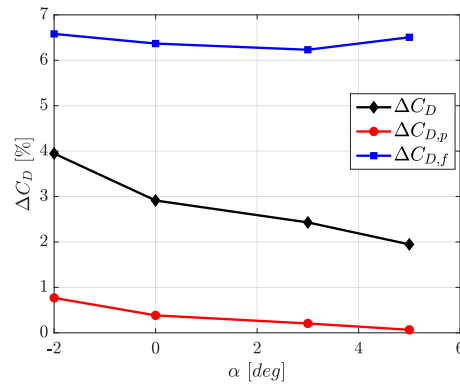
Figure 13. Drag reduction rate vs. angle of attack. The largest drag reduction is achieved in cruise condition.
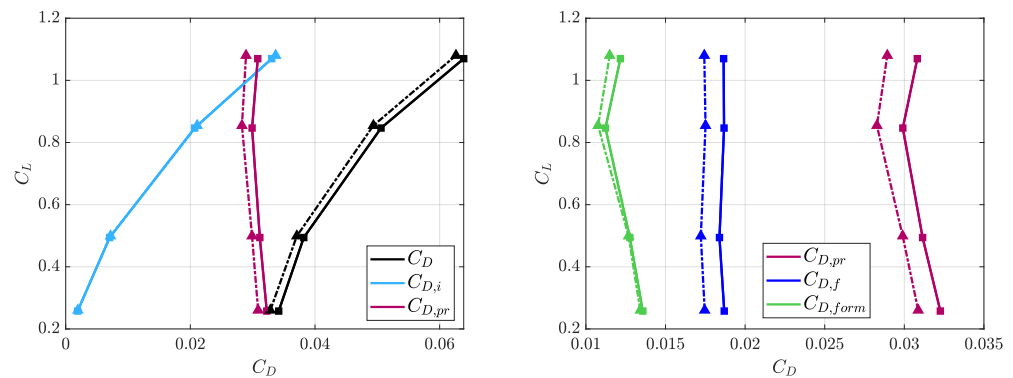

Figure 14. Drag breakdown (**left**) and decomposition of profile drag (**right**). Solid lines with square markers refer to clean configuration; dashed lines with triangular markers refer to riblets configuration.

4.3. Partial Coverage

Perhaps the most interesting consequence of the availability of a simple yet accurate boundary condition to model riblets within RANS simulations is the ability to carry out quick numerical studies to address practical problems related to their use. For example, since riblets produce limited benefits and imply costs and penalties, an elementary cost/benefit analysis should start by addressing the simple question of which area of the aircraft surface would yield the largest benefits after riblets installation. To this aim, we have designed a further set of simulations to explore partial coverage of the aircraft surface with riblets. The amount of coverage is quantified by the ratio β between the riblets-covered area and the total area, with $\beta = 1$ indicating total coverage. In these simulations, the full aircraft is considered, but riblets coverage varies according to Table 2, where case I is the full-coverage case described above. Outcomes of the simulations are shown in Table 3 and graphically represented in Figure 15. Figure 16 schematically illustrates where riblets are applied on the surface of the UAV.

Table 2. Coverage configurations.

	Riblets Deployment	β
I	Full coverage	1.000
II	No wing TE	0.953
III	No booms	0.935
IV	Only wing	0.524
V	Only wing, suction side	0.289

Table 3. Drag breakdown for the UAV in cruise condition, for different configurations of riblets coverage, and percentage changes with the clean case.

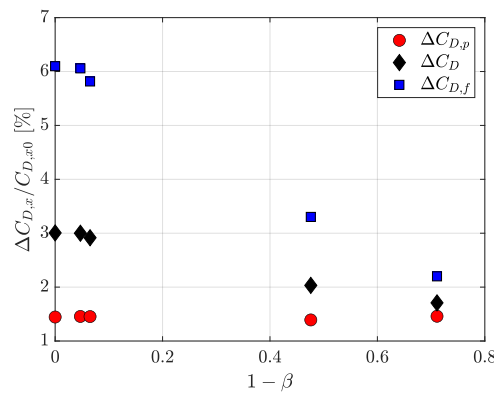|	C_D	$\Delta C_D/C_{D,0}\%$	$C_{D,p}$	$\Delta C_{D,p}/C_{D,p0}\%$	$C_{D,f}$	$\Delta C_{D,f}/C_{D,f0}\%$
Clean	**0.0508**	**-**	**0.0338**	**-**	**0.0170**	**-**
I	0.0493	3.0	0.0333	1.5	0.0160	6.1
II	0.0493	3.0	0.0333	1.5	0.0160	6.1
III	0.0493	2.9	0.0333	1.5	0.0160	5.8
IV	0.0498	2.0	0.0333	1.4	0.0165	3.3
V	0.0499	1.7	0.0333	1.5	0.0167	2.2

Figure 15. Drag reduction contributions for different configurations of riblets coverage from highest (I-full coverage) to lowest (V-wing only, suction side) coverage.

Since, at the trailing edge of the wing, riblets do not provide significant reductions in skin friction (Figure 11) while locally enforcing a substantial change from the optimal size, in configuration II riblets are removed from the trailing edge of the entire wing. The reduction of the riblets-covered surface is minimal (less than 5%) but, as expected, there is no appreciable decrease in terms of performance. Configuration III has riblets removed from the booms that connect the wing to the tail. Again, the overall drag reduction is essentially unchanged, with 6.5% savings in covered areas: pressure drag reduction remains unchanged since the boom is not an aerodynamic body, whereas friction reduction decreases, but minimally so, because the surface of the boom is small. Together, cases II and III suggest that removing riblets from both the trailing edge and the booms would avoid difficult areas, and save over 10% of application surface without incurring insignificant performance degradation.
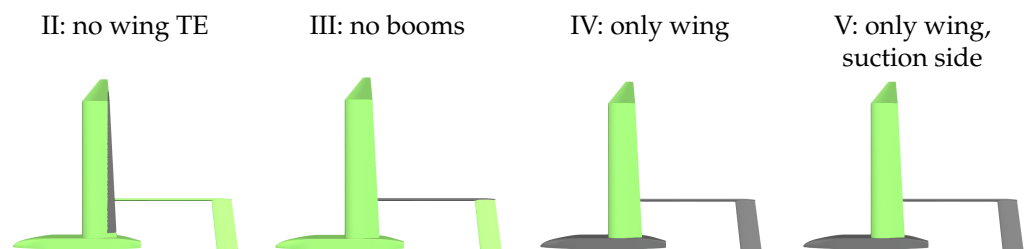

Figure 16. Schematic drawing of various riblets coverage configurations, cases II–V.

Configuration IV has riblets applied on the wing only, and is motivated by the observation that, in this application, pressure drag is approximately 2/3 of the whole drag, and that riblets placed on the wing produce pressure drag reduction in addition to friction drag reduction. With configuration IV, performance indeed degrades from 3% to 2%, but the saving in coverage area is more than proportional, with riblets surface shrinking down to one half at $\beta = 0.524$. As expected, pressure drag reduction remains almost unchanged at

1.4%, and friction drag reduction is seen to diminish from 6.1% to 3.3%: indeed, the area of the wing is approximately one half of the total area. Perhaps the most interesting configuration is configuration V, where only the suction side of the wing (and the entire winglet) is equipped with riblets, leading to $\beta = 0.289$. In contrast, the riblets-induced benefit remains more than one half, i.e., 1.7% instead of 3.0%.

5. Conclusions

The drag reduction potential of riblets deployed on a fixed-wing, low-speed Unmanned Air Vehicle (UAV) has been assessed with RANS simulations, with the aim of determining an optimal coverage policy. While riblets are fully characterised in low-speed flows over plane walls, and studies are available for aeronautical configurations in transonic flow (commercial mid- or long-range passenger aircraft), a low-speed aircraft such as the present one (for which the cruise speed is only 22 m/s) is considered here for the first time. Since the friction component of the aerodynamic drag of the UAV is modest, the effectiveness of riblets in this specific application needs to be assessed.

The RANS simulations, which employ a standard OpenFOAM setup, are unable to describe riblets directly. Thus, the presence of riblets is accounted for via a suitable slip condition enforced at the planar wall. The chosen amount of slip is constant in viscous units, and corresponds to riblets that locally possess optimal size in viscous wall units. The slip length model has been validated in the simple flows over a flat plate and around a subsonic airfoil, where results agree with available information.

Once applied to the UAV, the simulated riblets have brought out indirect and favourable effects, which go beyond the local reduction of friction drag, and also render the deployment of a friction-reduction device definitely interesting in such a low-speed application. Indeed, riblets significantly change the pressure distribution across the wing of the aircraft, which translates into an additional reduction of form drag, and in a lift increment as well. Although the latter obviously causes an increase in lift-induced drag, the requirement for the aircraft in cruise to fly at a given lift leads to a reduced angle of attack, and thus, to a further contribution to drag reduction. In the end, riblets provide up to 3% reduction of the total drag of the aircraft at cruise speed: a noticeable result, especially when the low-flight Reynolds number of the UAV is considered.

Once a cheap computational model is available to reliably compute the global effect of riblets on the aerodynamic drag, varying the riblets coverage policy becomes a computationally affordable task; relatively inexpensive simulations can help determine what drag benefit can be achieved with a given extent and location of the coverage of the aircraft surface. Thanks to the importance of secondary effects on pressure drag reduction induced by riblets, as a consequence of the significant pressure drag component, up to 1.7% of total drag reduction is achieved by placing riblets on the upper surface of the wing only. In this configuration, the total drag reduction is almost 2/3 of the maximum obtained with full coverage, but it is obtained with a coverage of less than 1/3 of the total area. Since riblets costs (for application and maintenance) are directly linked to the amount of riblets-covered surface, the wing-only configuration offers a reduced cost–benefit ratio, and does not touch the UAV fuselage, where systems (sensors, cameras, and transmitters) are designed to be installed. Further analysis can determine the practicality of riblets removal from high-wear areas (e.g., the leading edge), which would further add to the practical appeal of riblets in this application. Such calculations are made possible by the simplicity of the slip-length model, whose validity goes beyond riblets, since it can be used to simulate a generic drag-reducing device which locally reduces the skin friction.

Author Contributions: Conceptualization and methodology, C.M. and M.Q.; software and validation, C.B., L.C. and B.M.; writing—original draft preparation, C.B. and L.C.; writing—review and editing, F.G. and M.Q.; data curation, F.G.; supervision, M.Q.; project administration, C.M. All authors have read and agreed to the published version of the manuscript.

Data Availability Statement: The data presented in this study are available on request from the corresponding author.

Conflicts of Interest: The authors declare no conflicts of interest.

References

1. García-Mayoral, R.; Jiménez, J. Drag Reduction by Riblets. *Philos. Trans. R. Soc. A* **2011**, *369*, 1412–1427. [CrossRef] [PubMed]
2. Walsh, M.J.; Weinstein, L.M. Drag and Heat-Transfer Characteristics of Small Longitudinally Ribbed Surfaces. *AIAA J.* **1979**, *17*, 770–771. [CrossRef]
3. Bechert, D.; Bruse, M.; Hage, W.; Hoeven, J.V.D.; Hoppe, G. Experiments on Drag-Reducing Surfaces and Their Optimization with an Adjustable Geometry. *J. Fluid Mech.* **1997**, *338*, 59–87. [CrossRef]
4. Bechert, D.; Bartenwerfer, M. The Viscous Flow on Surfaces with Longitudinal Ribs. *J. Fluid Mech.* **1989**, *206*, 105–209. [CrossRef]
5. Luchini, P.; Manzo, F.; Pozzi, A. Resistance of a Grooved Surface to Parallel Flow and Cross-Flow. *J. Fluid Mech.* **1991**, *228*, 87–109. [CrossRef]
6. Luchini, P. Reducing the Turbulent Skin Friction. In *Computational Methods in Applied Sciences 1996*; Wiley: Hoboken, NJ, USA, 1996.
7. Spalart, P.; McLean, J. Drag Reduction: Enticing Turbulence, and Then an Industry. *Philos. Trans. R. Soc. A* **2011**, *369*, 1556–1569. [CrossRef] [PubMed]
8. Gatti, D.; Quadrio, M. Reynolds-Number Dependence of Turbulent Skin-Friction Drag Reduction Induced by Spanwise Forcing. *J. Fluid Mech.* **2016**, *802*, 553–558. [CrossRef]
9. Aupoix, B.; Pailhas, G.; Houdeville, R. Towards a General Strategy to Model Riblet Effects. *AIAA J.* **2012**, *50*, 708–716. [CrossRef]
10. Mele, B.; Tognaccini, R.; Catalano, P. Performance Assessment of a Transonic Wing-Body Configuration with Riblets Installed. *J. Aircr.* **2016**, *53*, 129–140. [CrossRef]
11. Koepplin, V.; Herbst, F.; Seume, J.R. Correlation-Based Riblet Model for Tubomachinery Applications. *J. Turbomach.* **2017**, *139*, 071006. [CrossRef]
12. Nieuwstadt, F.T.M.; Wolthers, W.; Leijdens, H.; Krishna Prasad, K.; Schwarz-van Manen, A. The Reduction of Skin Friction by Riblets under the Influence of an Adverse Pressure Gradient. *Exp. Fluids* **1993**, *15*, 17–26. [CrossRef]
13. Debisschop, J.; Nieuwstadt, F. Turbulent Boundary Layer in an Adverse Pressure Gradient: Effectiveness of Riblets. *AIAA J.* **1996**, *34*, 932–937. [CrossRef]
14. Boomsma, A.; Sotiropoulos, F. Riblet Drag Reduction in Mild Adverse Pressure Gradient: A Numerical Investigation. *Int. J. Heat Luid Flow* **2015**, *56*, 251–260. [CrossRef]
15. Mele, B.; Tognaccini, R. Slip Length–Based Boundary Condition for Modeling Drag Reduction Devices. *AIAA J.* **2018**, *56*, 3478–3490. [CrossRef]
16. Banchetti, J.; Luchini, P.; Quadrio, M. Turbulent Drag Reduction over Curved Walls. *J. Fluid Mech.* **2020**, *896*, 1–23. [CrossRef]
17. Quadrio, M.; Chiarini, A.; Gatti, D.; Banchetti, J.; Memmolo, A.; Pirozzoli, S. Drag Reduction on a Transonic Airfoil. *J. Fluid Mech.* **2022**, *in press*. [CrossRef]
18. Luchini, P. Linearized No-Slip Boundary Conditions at a Rough Surface. *J. Fluid Mech.* **2013**, *737*, 349–367. [CrossRef]
19. Gomez-de-Segura, G.; Fairhall, C.; MacDonald, M.; Chung, D.; Garcia-Mayoral, R. Manipulation of Near-Wall Turbulence by Surface Slip and Permeability. *J. Phys.* **2018**, *1001*, 012011. [CrossRef]
20. Walsh, M. Drag Characteristics of V-Groove and Transverse Curvature Riblets. In *Symposium on Viscous Flow Drag Reduction*; GR Hough American Institute of Aeronautics and Astronautics: New York, NY, USA, 1980.
21. Mele, B.; Tognaccini, R.; Catalano, P.; de Rosa, D. Effect of Body Shape on Riblets Performance. *Phys. Rev. Fluids* **2020**, *5*, 124609. [CrossRef]
22. Zhang, Z.; Zhang, M.; Cai, C.; Kang, K. A General Model for Riblets Simulation in Turbulent Flows. *Int. J. Comput. Fluid Dyn.* **2020**, *34*, 333–345. [CrossRef]
23. Catalano, P.; de Rosa, D.; Mele, B.; Tognaccini, R.; Moens, F. Performance Improvements of a Regional Aircraft by Riblets and Natural Laminar Flow. *J. Aircr.* **2020**, *57*, 29–40. [CrossRef]
24. Walsh, M.J.; Sellers, L.W.; McGinley, C.B. Riblet Drag at Flight Conditions. *J. Aircr.* **1989**, *26*, 570–575. [CrossRef]
25. McLean, J.; George-Falvy, D.; Sullivan, P. Flight Test of Turbulent Skin-Friction Reduction by Riblets. In *Proceedings of the RAeS International Conference on Turbulent Drag Reduction by Passive Means*; Royal Aeronautical Society: London, UK, 1987; Volume RAeS 2, pp. 408–424.
26. Szodruch, J. Viscous Drag Reduction on Transport Aircraft. In Proceedings of the 29th Aerospace Sciences Meeting, Reno, NV, USA, 7–10 January 1991; Aerospace Sciences Meetings; American Institute of Aeronautics and Astronautics: Reston, VI, USA, 1991. [CrossRef]
27. Kurita, M.; Nishizawa, A.; Kwak, D.; IIjima, H.; IIjima, Y.; Takahashi, H.; Sasamori, M.; Abe, H.; Koga, S.; Nakakita, K. Flight Test of a Paint-Riblet for Reducing Skin Friction. In Proceedings of the AIAA 2018 Applied Aerodynamics Conference, Atlanta, GA, USA, 25–29 June 2018; pp. 1–7. [CrossRef]
28. Kurita, M.; Iijima, H.; Koga, S.; Nishizawa, A.; Kwak, D.; Iijima, Y.; Takahashi, H.; Abe, H. Flight Test for Paint Riblets. In Proceedings of the AIAA Scitech 2020 Forum, Orlando, FL, USA, 6–10 January 2020. [CrossRef]
29. Luchini, P. Universality of the Turbulent Velocity Profile. *Phys. Rev. Lett.* **2017**, *118*, 224501. [CrossRef] [PubMed]

30. Weller, H.; Tabor, G.; Jasak, H.; Fureby, C. A Tensorial Approach to Computational Continuum Mechanics Using Object-Oriented Techniques. *Comput. Phys.* **1998**, *12*, 620–631. [CrossRef]
31. Menter, F. Two-Equation Eddy-Viscosity Turbulence Models for Engineering Applications. *AIAA J.* **1994**, *32*, 1598–1605. [CrossRef]
32. Mele, B.; Tognaccini, R. Numerical Simulation of Riblets on Airfoils and Wings. In Proceedings of the 50th AIAA Aerospace Sciences Meeting including the New Horizons Forum and Aerospace Exposition, Nashville, TN, USA, 9–12 January 2012; American Institute of Aeronautics and Astronautics: Reston, VI, USA, 2012.
33. Ladson, C.L. *Effects of Independent Variation of Mach and Reynolds Numbers on the Low-Speed Aerodynamic Characteristics of the NACA 0012 Airfoil Section*; NASA TM 4074; NASA: Washington, DC, USA, 1988.
34. Sundaram, S.; Viswanath, P.; Rundrakumar, S. Viscous Drag Reduction Using Riblets on NACA 0012 Airfoil to Moderate Incidence. *AIAA J.* **1996**, *34*, 676–682. [CrossRef]
35. Viswanath, P. Aircraft Viscous Drag Reduction Using Riblets. *Prog. Aerosp. Sci.* **2002**, *38*, 571–600. [CrossRef]